NASA/TM-2007-214611

Guidance and Control of an Autonomous Soaring UAV

Michael J. Allen
NASA Dryden Flight Research Center
Edwards, California

February 2007

NASA STI Program ... in Profile

Since its founding, NASA has been dedicated to the advancement of aeronautics and space science. The NASA scientific and technical information (STI) program plays a key part in helping NASA maintain this important role.

The NASA STI program is operated under the auspices of the Agency Chief Information Officer. It collects, organizes, provides for archiving, and disseminates NASA's STI. The NASA STI program provides access to the NASA Aeronautics and Space Database and its public interface, the NASA Technical Report Server, thus providing one of the largest collections of aeronautical and space science STI in the world. Results are published in both non-NASA channels and by NASA in the NASA STI Report Series, which includes the following report types:

- TECHNICAL PUBLICATION. Reports of completed research or a major significant phase of research that present the results of NASA programs and include extensive data or theoretical analysis. Includes compilations of significant scientific and technical data and information deemed to be of continuing reference value. NASA counterpart of peer-reviewed formal professional papers but has less stringent limitations on manuscript length and extent of graphic presentations.

- TECHNICAL MEMORANDUM. Scientific and technical findings that are preliminary or of specialized interest, e.g., quick release reports, working papers, and bibliographies that contain minimal annotation. Does not contain extensive analysis.

- CONTRACTOR REPORT. Scientific and technical findings by NASA-sponsored contractors and grantees.

- CONFERENCE PUBLICATION. Collected papers from scientific and technical conferences, symposia, seminars, or other meetings sponsored or cosponsored by NASA.

- SPECIAL PUBLICATION. Scientific, technical, or historical information from NASA programs, projects, and missions, often concerned with subjects having substantial public interest.

- TECHNICAL TRANSLATION. English-language translations of foreign scientific and technical material pertinent to NASA's mission.

Specialized services also include creating custom thesauri, building customized databases, and organizing and publishing research results.

For more information about the NASA STI program, see the following:

Access the NASA STI program home page at *http://www.sti.nasa.gov.*

- E-mail your question via the Internet to help@sti.nasa.gov.

- Fax your question to the NASA STI Help Desk at (301) 621-0134.

- Phone the NASA STI Help Desk at (301) 621-0390.

- Write to:
  NASA STI Help Desk
  NASA Center for AeroSpace Information
  7115 Standard Drive
  Hanover, MD 21076-1320

NASA/TM-2007-214611

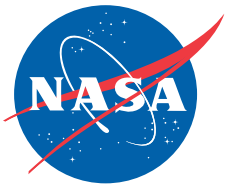

Guidance and Control of an Autonomous Soaring UAV

Michael J. Allen
NASA Dryden Flight Research Center
Edwards, California

National Aeronautics and
Space Administration

Dryden Flight Research Center
Edwards, California 93523-0273

February 2007

Cover art: NASA Dryden Flight Research Center, photograph EC05-0198-08.

Available from:

NASA Center for AeroSpace Information
7115 Standard Drive
Hanover, MD 21076-1320
(301) 621-0390

ABSTRACT

Thermals caused by convection in the lower atmosphere are commonly used by birds and glider pilots to extend flight duration, increase cross-country speed, improve range, or simply to conserve energy. Uninhabited Aerial Vehicles (UAVs) can also increase performance and reduce energy consumption by exploiting atmospheric convection. An autonomous soaring research project was conducted at the NASA Dryden Flight Research Center to evaluate the concept through flight test of an electric-powered motor-glider with a wingspan of 4.27 m (14 ft). The UAV's commercial autopilot software was modified to include outer-loop soaring guidance and control. The aircraft total energy state was used to detect and soar within thermals. Estimated thermal size and position were used to calculate guidance commands for soaring flight. Results from a total of 23 thermal encounters show good performance of the guidance and control algorithms to autonomously detect and exploit thermals. The UAV had an average climb of 172 m (567 ft) during these encounters.

NOMENCLATURE

a	equatorial radius of the earth, m
dt_q	queue sample time step, s
E	total specific energy of the aircraft, m
$\dot{E}$	specific energy rate, m/s
$\dot{E}_{motor}$	specific energy rate due to the motor, m/s
$\dot{E}_{pf}$	post flight estimated specific energy rate, m/s
$\ddot{E}$	specific energy acceleration, m/s^2
$\ddot{E}_s$	scaled specific energy acceleration, m/s^2
e_p	controller position error, m
e_{sumsq}	mean sum squared velocity error, m^2/s^2
e_v	controller velocity error, m/s
e_w	weighted velocity error, m/s
$\hat{e}_{sumsq}$	mean sum squared velocity error for perturbed thermal radius, m^2/s^2
$\hat{e}_w$	weighted velocity error for perturbed thermal radius, m/s
g	gravitational constant of Earth, m/s^2
H_q	velocity influence vector
h_{est}	estimated aircraft altitude, m
i_q	queue index
k	current measurement index
k_1	energy acceleration gain, deg*s/m
k_2	position error gain, deg/m*s
k_3	velocity error gain, deg/m

L_r	learning rate, $1/s^2$
Lat	latitude of aircraft, rad
Lat_0	latitude of X Y reference frame, rad
Lon	longitude of aircraft, rad
Lon_0	longitude of X Y reference frame, rad
M_D	number of rows used in drift calculation
M_q	number of rows in the queue
m	aircraft mass, kg
P	aircraft position, m
P_{th}	estimated thermal position, m
P_{thD_1}	thermal position calculated from the first 20 entries in the queue, m
P_{thD_2}	thermal position calculated from the last 20 entries in the queue, m
P_X	aircraft X position, m
P_Y	aircraft Y position, m
p_{static}	static pressure, Pa
q_s	queue of aircraft position and shifted energy rate
q_1	queue of aircraft position and energy rate
q_2	queue of drift corrected aircraft position and energy rate
r_{cmd}	radius of commanded circular flight path, m
r_{th}	estimated thermal radius, m
$\hat{r}_{th}$	perturbed thermal radius, m
Soarmode	mode logic state
S	distance between the aircraft and the thermal center, m
s	Laplace transform variable
T	thrust from the motor, N
$T_{\max}$	maximum thrust from the motor, N
$throt_{t-1}$	one-second delayed throttle command, fraction
$throt_{trim}$	trim throttle needed for level flight, fraction
V	true airspeed, m/s
V_D	estimated thermal drift velocity, m/s
V_e	sink rate of the air between thermals (environment sink rate), m/s
$\dot{V}_{motor}$	estimated aircraft velocity rate caused by the motor, m/s^2
w_{pred}	predicted thermal vertical velocity, m/s
w_{th}	estimated thermal vertical velocity, m/s
$\hat{w}_{pred}$	predicted thermal vertical velocity for perturbed thermal radius, m/s

δ_r	thermal radius stepsize, m
Δ_r	perturbed thermal radius error gradient, m/s^2
$\dot{\psi}_{cmd}$	turn rate command, deg/s
$\dot{\psi}_{ss}$	steady state turn rate, deg/s

INTRODUCTION

A novel way to improve the range, duration, or cross-country speed of an autonomous aircraft is to use buoyant plumes of air called thermals. Thermals occur when the air near the ground becomes less dense than the surrounding air as a result of heating or humidity changes at the Earth's surface. Thermal height varies greatly depending on climate and season but can typically fall between 500 m (1600 ft) and 3700 m (12 000 ft) above ground level. Sailplane pilots primarily rely on thermals to travel great distances and soar for long periods of time (ref. 1). Large birds, such as hawks and buzzards, have been observed to soar extensively while searching for food and vary their migration path and flight times in response to thermal activity (refs. 2–4) and frigatebirds are known to soar continuously day and night using thermals over tropical ocean waters (ref. 5).

Many unmanned aerial vehicles (UAVs) have similar sizes and wing loadings to soaring birds and manned sailplanes. Mission profiles that could allow small UAVs to take advantage of thermals include remote sensing, surveillance, atmospheric research, communications, force protection, forest-fire monitoring, land management, and border control. A study using a simple UAV simulation with thermals calculated from meteorological data from Desert Rock, Nevada, found that a UAV with a nominal endurance of 2 hours can gain up to 12 hours of flight time by using thermals (ref. 6).

Many strategies for extracting energy from thermals and other atmospheric phenomena have been published for glider pilots (refs. 1 and 7). Autonomous soaring for UAVs is an emerging field of study. Boslough (ref. 8) used piloted flight tests with an instrumented model glider to investigate specific maneuvers flown in the presence of wind shear and proposed that flocks of soaring UAVs could radically increase the efficiency of powered flight. Patel showed through simulation that significant energy savings can be achieved for UAVs by performing pitch maneuvers in turbulent air (ref. 9). Autonomous thermal soaring UAVs were first proposed by Wharington (refs. 10 and 11) in 1998 as a method to extend UAV performance and possibly to enable perpetual flight. Optimal guidance algorithms were developed using reinforcement learning and a neural-based thermal locator to autonomously detect and utilize thermals. Results showed that both simple heuristics and reinforcement learning could be used along with the thermal locator to improve UAV performance, but the reinforcement learning algorithms were too computationally intensive for real-time use. A less complex autonomous soaring autopilot developed by Staffan Kjerrström (ref. 12) has been used by autonomous gliders to detect and use thermals to gain altitude. The autopilot has been hosted on a number of model glider airframes with mixed results. During the summer of 2005, Alan Cocconi demonstrated high-endurance flight of a small UAV by flying his 4.27-m (14-ft) span solar powered motor-glider continuously for 48 hours (refs. 13–15). Autonomous soaring was not employed on this flight. Instead, experienced pilots guided the aircraft to soar in

thermals. The flight showed that a flight lasting multiple days with a small electric-powered UAV is possible using solar power and thermal soaring.

A research project conducted by the NASA Dryden Flight Research Center (Edwards, California) developed and tested autonomous soaring algorithms using the small UAV shown in figure 1. The single objective of the project was to flight test a set of algorithms designed to autonomously detect and utilize thermals for energy gain. The autonomous soaring algorithms were hosted on a Piccolo Plus autopilot (CloudCap Technology, Hood River, Oregon) as an outer-loop guidance module computed 20 times per second. An SBXC (RnR Products, Milpitas, California) radio-controlled cross-country glider was chosen for flight tests because of its considerable fuselage capacity and excellent gliding performance. The aircraft was modified to include a flight termination system, a Piccolo Plus autopilot, a pitot-static probe, antennas, an electric motor, and a folding propeller. The resulting UAV, dubbed the Cloud Swift, has a lift-to-drag ratio of approximately 28 and a minimum sink rate of approximately 0.4 m/s as determined from flight.

EC05-0198-08

Figure 1. The Cloud Swift UAV. The Cloud Swift is a modified SBXC glider (RnR Products) and has a span of 4.27 m (14 ft) and a weight of 6.8 kg (15 lb).

AUTONOMOUS SOARING GUIDANCE AND CONTROL

The top-level autonomous soaring guidance and control structure is shown in figure 2. The guidance and control for soaring are implemented as an outer-loop controller to the Piccolo Plus autopilot. Inputs to the soaring guidance and control consist of static pressure, airspeed, throttle command, and the latitude and longitude of the aircraft. Estimates of the total energy rate and total energy acceleration of the aircraft are used by the thermal identification equations to determine the radius, vertical velocity, and position of the thermal. The circle guidance calculates the steady-state turn rate, position error, and velocity error for tracking a circular path inside the thermal. The controller attempts to drive position and velocity errors to zero and respond to changes in energy acceleration. Finally, mode logic uses aircraft energy terms to determine when the aircraft should be searching for thermals (by flying waypoints) and when it should circle within a thermal.

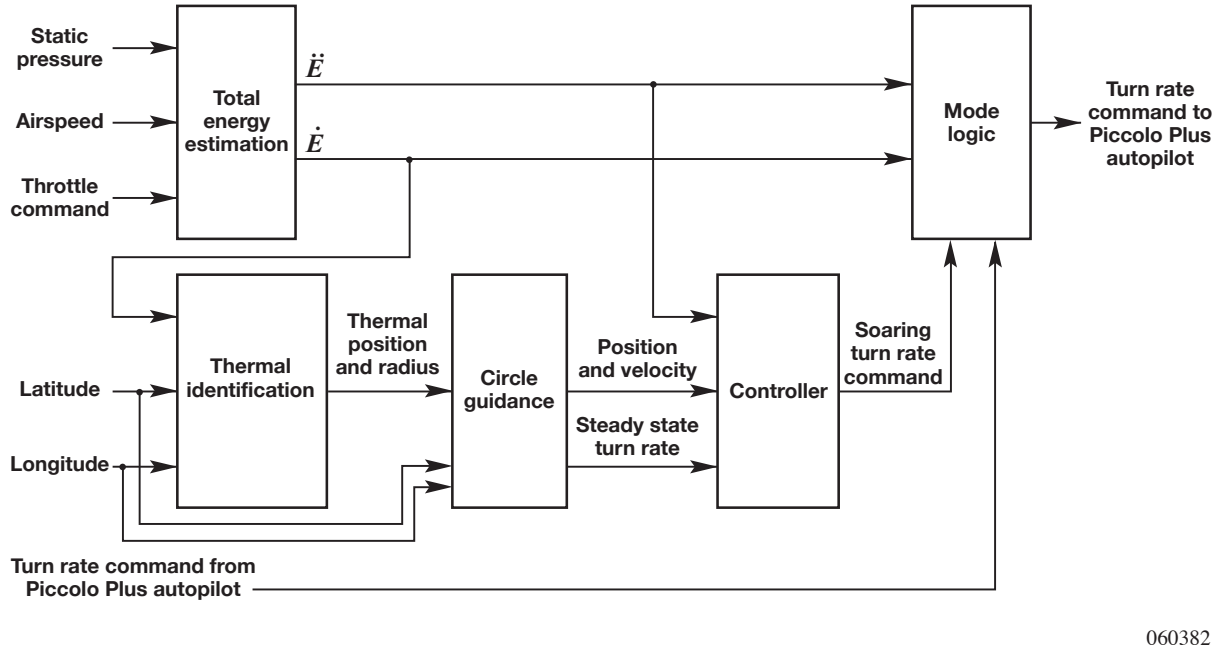

Figure 2. Top level block diagram of autonomous soaring guidance and control.

Total Energy Estimation

Static pressure sensor input, estimated true airspeed, and the aircraft throttle command were used to determine the rate and acceleration of aircraft total energy. The energy rate and acceleration define the basic parameters that are used to guide the aircraft during soaring flight. Aircraft total specific energy was first calculated by collecting the potential and kinetic energy terms of the aircraft energy equation normalized by aircraft weight. The resulting energy term, E , is referred to as total energy in this paper and was calculated using eq. (1).

$$E = h_{est} + \frac{V^2}{2g} \tag{1}$$

Equation (1) is solved using gravity, g, airspeed, V, and the estimated aircraft altitude, h_{est}, from a representation of the standard atmosphere (ref. 16). Equation (2) gives a reasonable fit to the standard atmosphere for altitudes below 10 000 m.

$$h_{est} = \left[1 - \left(\frac{p_{static}}{101325}\right)^{0.1903}\right] 44333.7 \tag{2}$$

An approximate pressure altitude estimate was adequate for autonomous soaring because only the rate of change of energy is used by the guidance and control. The total energy calculations are illustrated in figure 3. Total energy was filtered and differentiated with filter 1 and filter 2 to obtain specific energy rate, $\dot{E}$.

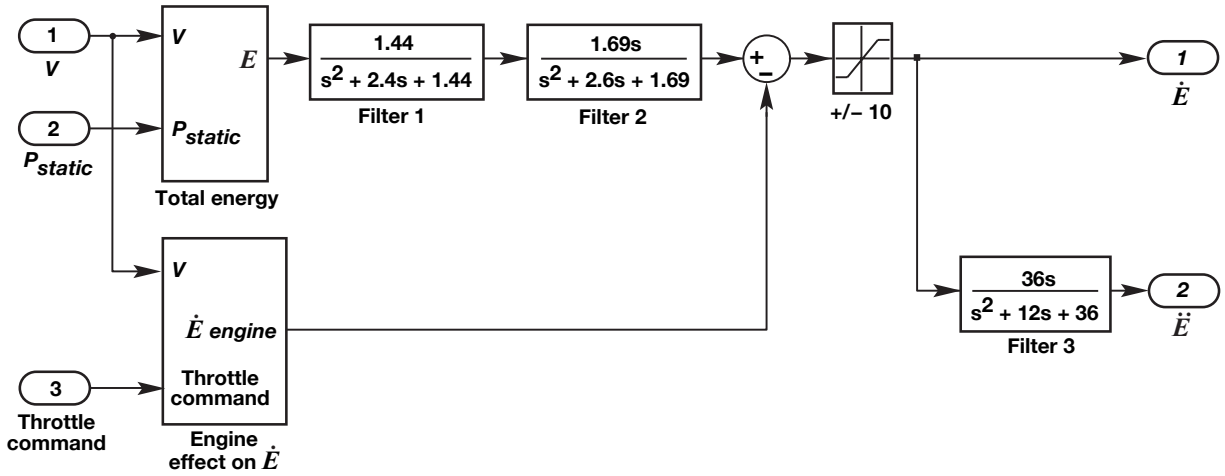

060383

Figure 3. Total energy estimation.

Energy rate was corrected to account for the energy added to the aircraft by the motor. The correction term was calculated by differentiating eq. (1) and solving for motor terms only. The resulting relationship is given in eq. (3).

$$\dot{E}_{motor} = \frac{V\dot{V}_{motor}}{g} \tag{3}$$

Equation (3) was solved using an approximation of $\dot{V}_{motor}$ given in eq. (4)

$$\dot{V}_{motor} = \frac{T}{m} \tag{4}$$

where T is the axial force from the motor and m is the aircraft mass. Thrust is calculated from the simple engine model given in eq. (5)

$$T = \frac{0.64\left(throt_{t-1} - throt_{trim}\right)T_{\max}}{s^2 + 0.16s + 0.64} \tag{5}$$

where $throt_{t-1}$ is the 1-s delayed throttle command and $throt_{trim}$ is the trim throttle needed for level flight. The term $T_{\max}$ is the maximum thrust generated by the motor. One second was chosen for the throttle delay to account for delay in the motor and speed controller systems and to approximate the delay in the $\dot{E}$ calculation. Equation (5) is essentially a gain of $T_{\max}$ on the change in delayed throttle command delta from trim throttle and a second-order filter with a 0.8 rad/s cutoff frequency. Values for $T_{\max}$ and $throt_{trim}$ were taken from flight data. The estimated energy rate was rate-limited at ±10 m/s^2 to reduce transient behavior.

Filter 3, shown in figure 3 was used to calculate energy acceleration, $\ddot{E}$. Finally, energy acceleration was modified to produce scaled energy acceleration, $\ddot{E}_s$, using eq. (6).

$$\ddot{E}_s = \frac{\ddot{E}}{\max(\dot{E}, 1.0)} \tag{6}$$

Scaling was used to reduce the sensitivity of the controller to variations in thermal strength. The use of scaled energy acceleration allowed the soaring controller to behave similarly while flying in weak lift with small variations in energy acceleration or flying in strong lift with large variations in energy acceleration.

The three filters used in the total energy calculations have two purposes. First, the filters must remove noise from the aircraft energy acceleration estimate that is caused by imperfect pressure sensor accuracy and resolution. Second, the filters must twice differentiate total energy to produce energy acceleration. The undesired effect of this method is a high time delay. This estimation latency reduced the effectiveness of the $\ddot{E}$ feedback channel in the controller and was the primary reason for the development of the thermal identification algorithms. Possible ways to reduce delay in future soaring algorithms include the use of better sensors, higher-order filters, or incorporation of aircraft acceleration into the energy state estimation equations.

Thermal Identification

An estimation of the thermal location, size, and strength was made to improve soaring performance. The top level block diagram for the thermal estimation is given in figure 4. The aircraft position, P, was calculated in Cartesian coordinates from the latitude and longitude using eqs. (7) and (8).

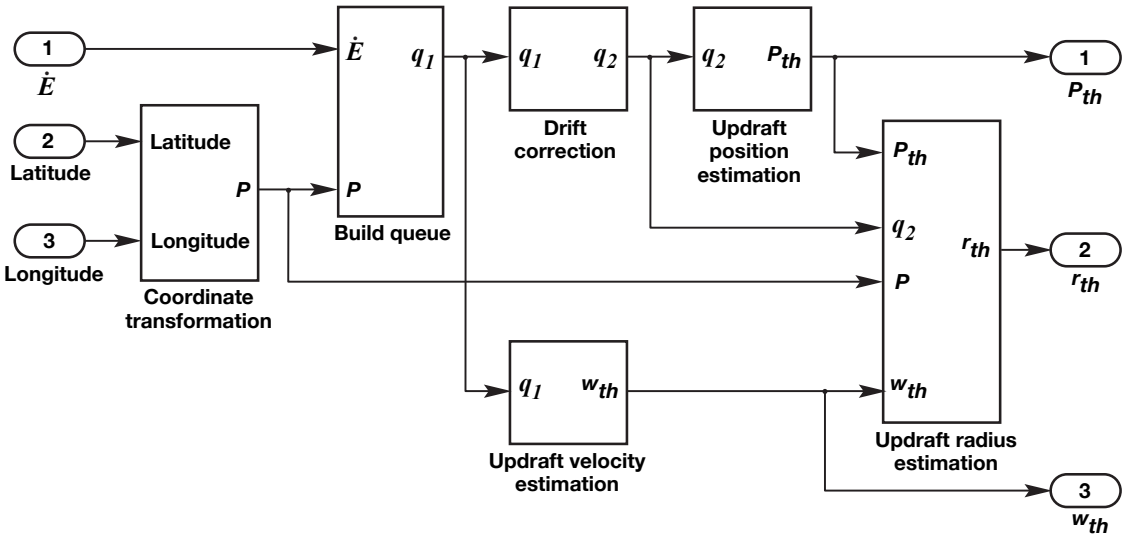

Figure 4. Thermal estimation top level block diagram.

$$P_X = \left(Lat - Lat_0\right)a \tag{7}$$

$$P_Y = \left(Lon - Lon_0\right)a\cos\left(Lat_0\right) \tag{8}$$

Equations (7) and (8) are solved using the equatorial radius of the Earth, a, the aircraft latitude and longitude, Lat and Lon, and the latitude and longitude of the chosen origin location, Lat_0 and Lon_0 (such as the location of the UAV ground station).

A history of previous aircraft positions and energy rates was collected in a first-in-first-out queue, given by eq. (9).

$$q_1 = \begin{bmatrix} P_{X_k} & P_{Y_k} & \dot{E}_k \\ P_{X_{k-1}} & P_{Y_{k-1}} & \dot{E}_{k-1} \\ \vdots & \vdots & \vdots \\ P_{X_{k-M_q+1}} & P_{Y_{k-M_q+1}} & \dot{E}_{k-M_q+1} \end{bmatrix} \tag{9}$$

Entries to the queue given in eq. (9) were made using a queue sample time step, dt_q, of 1 s. The subscript k refers to the measurement index. The length of the queue, M_q, used in eq. (9) was chosen to be 45 samples because the aircraft roughly completes 2 circles in that time.

Estimation of the movement or drift of the thermal was found through flight test to be important for achieving a good estimate of thermal position and radius. Drift is primarily caused by wind, but early flight tests showed that thermals do not always drift with the same velocity or direction as the prevailing winds. A discussion on thermal drift with possible reasons why it is not equal to the wind velocity is given in reference 17. Thermal drift was calculated by comparing the position of the thermal given by the first M_D entries of the queue with the position of the thermal given by the last M_D entries of the queue.

First, the energy rate entries of the queue were shifted using eqs. (10a) and (10b) to prevent negative values from entering subsequent calculations.

$$q_s\left(i_q,\left[1,2\right]\right) = q_1\left(i_q,\left[1,2\right]\right) \tag{10a}$$

$$q_s\left(i_q,3\right) = q_1\left(i_q,3\right) - \min\left(q_1\left(:,3\right)\right) \tag{10b}$$

Equation (10) produces the shifted queue, q_s, where the term $q_1\left(:,3\right)$ represents the third column of q_1. The thermal position given by the first or most recent M_D rows of q_s was calculated using eq. (11).

$$P_{thD_1} = \begin{bmatrix} \dfrac{\sum_{i_q=1}^{M_D} q_s(i_q,1)q_s(i_q,3)}{\sum_{i_q=1}^{M_D} q_s(i_q,3)} & \dfrac{\sum_{i_q=1}^{M_D} q_s(i_q,2)q_s(i_q,3)}{\sum_{i_q=1}^{M_D} q_s(i_q,3)} \end{bmatrix} \tag{11}$$

The thermal position given by the last M_D rows of q_s was calculated using eq. (12).

$$P_{thD_2} = \begin{bmatrix} \dfrac{\sum_{i_q=M_q-M_D-1}^{M_q} q_s(i_q,1)q_s(i_q,3)}{\sum_{i_q=M_q-M_D-1}^{M_q} q_s(i_q,3)} & \dfrac{\sum_{i_q=M_q-M_D-1}^{M_q} q_s(i_q,2)q_s(i_q,3)}{\sum_{i_q=M_q-M_D-1}^{M_q} q_s(i_q,3)} \end{bmatrix} \tag{12}$$

The estimated drift velocity of the thermal, V_D, was calculated from eq. (13)

$$V_D = \frac{P_{thD2} - P_{thD1}}{\left(M_q - M_D\right) * dt_q} \tag{13}$$

The resulting drift velocity was limited to ±10 m/s and rate limited to ±0.1 m/s^2. A restrictive rate limit was chosen to retain previous drift calculation information. The estimated drift velocity was then used to form a drift-corrected queue, q_2 , using eqs. (14a), (14b), and (14c).

$$q_2(i_q,1) = (i_q - 1)V_D\left(1\right) * dt_q + q_s(i_q,1) \tag{14a}$$

$$q_2(i_q,2) = (i_q - 1)V_D\left(2\right) * dt_q + q_s(i_q,2) \tag{14b}$$

$$q_2(i_q,3) = q_s(i_q,3) \tag{14c}$$

Figure 5 shows the mapping of aircraft position values in q_s to the positions given in q_2 to account for drift. Typical soaring flight data was used in this illustration. The result of the drift correction is to transform the aircraft position measurements into a reference frame that is moving with the thermal. The resulting queue, q_2 , can then be used to give a better real-time estimate of the thermal position and radius.

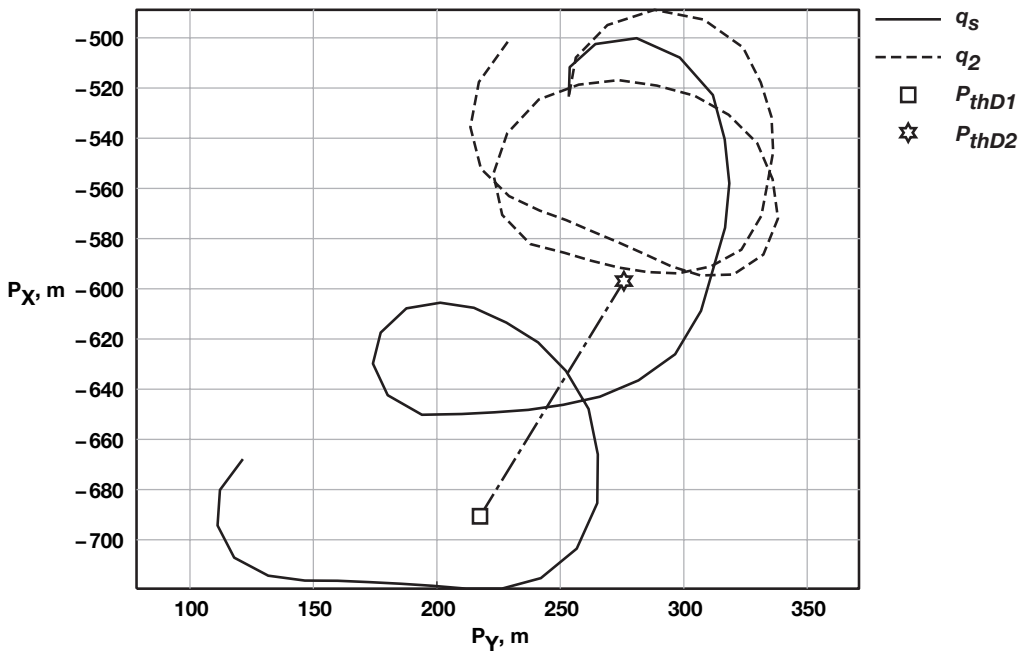

060385

Figure 5. Comparison of the queue q_s , before the drift correction, to the queue q_c , after the drift correction. Drift was calculated using P_{thD_1} and P_{thD_2} .

The estimated position of the thermal center, P_{th}, was calculated using the corrected queue, q_2, as given in eq. (15).

$$P_{th} = \begin{bmatrix} \dfrac{\sum_{i_q=1}^{M_q} q_2(i_q,1)q_2(i_q,3)^2}{\sum_{i_q=1}^{M_q} q_2(i_q,3)^2} & \dfrac{\sum_{i_q=1}^{M_q} q_2(i_q,2)q_2(i_q,3)^2}{\sum_{i_q=1}^{M_q} q_2(i_q,3)^2} \end{bmatrix} \tag{15}$$

Equation (15) represents the position centroid of the aircraft energy rate during the previous M_q samples. This method for estimating thermal position is easy to implement, does not require tuning, can be used for any thermal size, and does not have a high computational cost. Drawbacks associated with this method are sensitivity to the length of the queue and a bias of the estimated thermal position toward the mean position of the measurement set. The centroid calculations found in eq. (15) differ from the centroid calculations found in eqs. (11) and (12) because the energy rate term in the numerator is squared in eq. (15) to increase the sensitivity of the estimated thermal position to changes in energy rate.

Thermal vertical velocity, w_{th}, was approximated from the aircraft energy rate history found in q_1 using eq. (16).

$$w_{th} = 1.1\max(q_1(:,3)) \tag{16}$$

Equation (16) uses the assumption that the maximum thermal vertical velocity is 10 percent greater than the maximum energy rate experienced by the vehicle during the previous M_q samples. This very simple estimation method was used because high accuracy was not required. The thermal vertical velocity was rate limited to $+0.025$ m/s^2 and -0.015 m/s^2 as a method to retain old information about the thermal strength that has been passed from the queue. The estimated thermal vertical velocity was used in addition to the values in q_2 to estimate the thermal radius.

Thermal Radius Estimation

The radius of the thermal was estimated using a gradient descent method to fit an assumed thermal shape to the data found in the queue. The estimation process started with the calculation of the distance between each aircraft position in q_2 to the estimated thermal center, P_{th}, using eq. (17).

$$S(i_q) = \sqrt{\left(q_2(i_q,1) - P_{th}(1)\right)^2 + \left(q_2(i_q,2) - P_{th}(2)\right)^2} \tag{17}$$

The vector, S, was used to calculate the predicted thermal vertical velocity of each position in q_2 using the thermal vertical velocity distribution developed by Wharington (ref. 11) but modified here to account for the environment sink rate, V_e. The resulting shape is given in eq. (18).

$$w_{pred}\left(i_q\right) = \left(w_{th} + V_e\right) e^{-\left(\frac{S\left(i_q\right)}{\max(r_{th},1)}\right)^2} - V_e \tag{18}$$

Equation (18) was first solved using an initial value of 45 m for the estimated thermal radius, r_{th}, and estimated thermal radius from the previous frame thereafter. The shape of the predicted thermal vertical velocity distribution is plotted in figure 6. The radius of this shape is located at $w_{pred} / w_{th} = 0.24$, not at the zero crossing.

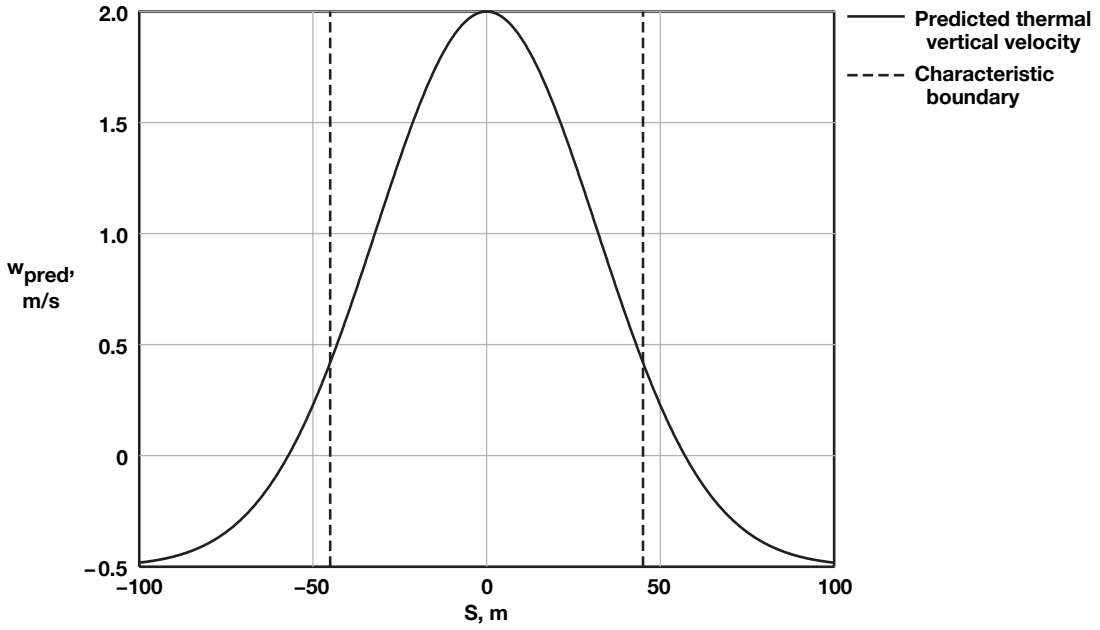

060386

Figure 6. Predicted thermal vertical velocity distribution from eq. (19) for w_{th} = 2 m/s and w_{th} = 45 m.

A weighted error, e_w, was calculated by taking the difference between the predicted thermal vertical velocity, w_{pred}, and the energy rate of the aircraft given in the third column of q_2. The weighted velocity error was calculated using eq. (19).

$$e_w(i_q) = \left(w_{pred}(i_q) - q_2(i_q,3)\right) H_q(i_q) \tag{19}$$

The velocity influence vector, H_q, was used to weight the more recent values of q_2 and w_{pred} higher than the older values. Values for H_q are plotted in figure 7.

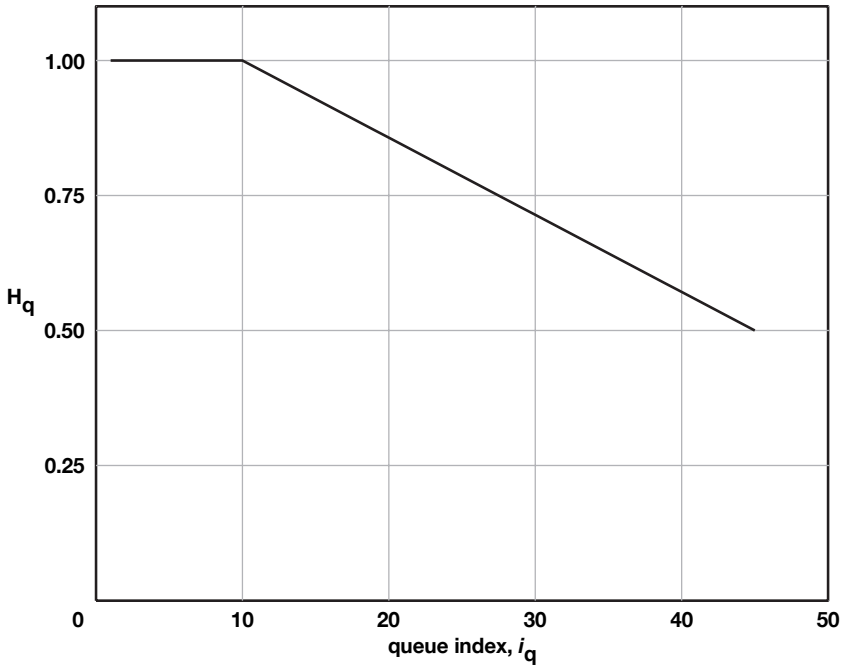

Figure 7. Influence vector, H_q, for a queue size, M_q, of 45. The influence vector was used to de-emphasize older data points.

The mean sum squared velocity error, e_{sumsq}, was calculated using eq. (20).

$$e_{sumsq} = \frac{e_w \bullet e_w}{M_q} \tag{20}$$

Equation (20) gives a measure of the fit between the assumed thermal shape given in eq. (18) and the measured energy rate of the aircraft stored in the queue. The sum squared velocity error for a perturbed radius, $\hat{e}_{sumsq}$, was calculated in a similar way using eqs. (21)–(23).

$$\hat{w}_{pred}\left(i_q\right) = \left(w_{th} + V_e\right) e^{-\left(\frac{S\left(i_q\right)}{\max(\hat{r}_{th},1)}\right)^2} - V_e \tag{21}$$

$$\hat{e}_w = \left(\hat{w}_{pred}\left(i_q\right) - q_c(i_q,3)\right) H_q\left(i_q\right) \tag{22}$$

$$\hat{e}_{sumsq} = \frac{\hat{e}_w \bullet \hat{e}_w}{M_q} \tag{23}$$

The perturbed radius, $\hat{r}_{th}$, used in eq. (21) is defined by eq. (24).

$$\hat{r}_{th} = r_{th} + \delta_r \tag{24}$$

The stepsize, δ_r, was chosen to be 0.5 m for this study because this value gave smooth and rapid convergence of the estimated thermal radius and was robust to thermal size variations.

The error for the current thermal radius and the error for the perturbed thermal radius were used to calculate a gradient as given in eq. (25).

$$\Delta_r = \frac{e_{sumsq} - \hat{e}_{sumsq}}{\delta_r} \tag{25}$$

The gradient was then used to calculate the thermal radius for the next frame using eq. (26)

$$r_{th_{k+1}} = L_r \Delta_r + r_{th_k} \tag{26}$$

with a learning rate, L_r, of 10. A learning rate of 10 was chosen because it gave rapid and smooth convergence of the estimated thermal radius with flight data. Estimated thermal radius was limited to be greater than 40 m to prevent soaring in small diameter thermals requiring high bank angle flight and to be less than 80 m to make the soaring algorithms more robust to variations of the position and strength of large thermals. Alternative methods for estimating thermal radius exist (ref. 11) but were not used here.

Guidance Calculations

Guidance calculations were used to determine the position error, velocity error, and the steady-state turn rate associated with flying in a circular path inside the thermal. The aircraft was commanded to fly a circular flight path having a radius, r_{cmd}, determined by eq. (27).

$$r_{cmd} = 0.65 r_{th} \tag{27}$$

The scale factor 0.65 was chosen because it defines a flight path radius that is usually small enough to be within the thermal "core" but large enough to avoid the high aircraft sink rate associated with high bank angle turns. The steady-state turn rate, $\dot{\psi}_{ss}$, needed to fly at an airspeed of V along a circular path given by r_{cmd} is given in eq. (28).

$$\dot{\psi}_{ss} = \left(\frac{-180}{\pi} \right) \left(\frac{V}{r_{cmd}} \right) \tag{28}$$

The negative sign in eq. (28) ensured that the aircraft always circled to the left while soaring. This was done to give the research personnel a quick visual indication of the aircraft mode during flight test. Flight plans were designed to command right turns when the aircraft was searching for thermals and left turns when the aircraft was in soaring mode. Future soaring guidance algorithms could potentially reduce the time needed to initially center a thermal by using the aircraft roll response to determine the turn direction as described in reference 1.

Controller position error, e_p, was generated using eq. (29).

$$e_p = r_{cmd} - S(1) \tag{29}$$

Position error was differentiated and filtered to create controller velocity error, e_v, using the transfer function given in eq. (30).

$$e_v = \frac{1.69s}{s^2 + 2.6s + 1.69} e_p \tag{30}$$

The guidance calculations given in eqs. (27)–(30) calculate the position error, velocity error, and steady-state turn rate information that was used by the soaring controller to maintain a circular flight path centered on the thermal.

Soaring Controller

The soaring controller architecture is loosely based on one of the thermal centering methods given for glider pilots by Reichmann (ref. 7). A paraphrase of Reichmann's method gives three rules:

1. As climb improves, flatten the circle (approximately 15–20° bank angle)
2. As climb deteriorates, steepen the circle (approximately 50° bank angle)
3. If climb remains constant, keep constant bank (approximately 25–30° bank angle)

These rules were used as a starting point for the soaring controller design shown in figure 8. Energy acceleration feedback was used to implement rules 1 and 2 because the rules given by Reichmann are to be applied to the "changes in rate of climb." The steady-state turn rate term kept the aircraft at a constant bank angle when the feedback terms were zero to fulfill rule 3. The soaring controller inputs consist of scaled energy acceleration, $\ddot{E}_s$, position error, e_p, velocity error, e_v, and steady state turn rate, $\dot{\psi}_{ss}$. The soaring controller output consists of a turn rate command, $\dot{\psi}_{cmd}$, that was sent to the autopilot. The energy acceleration gain, k_1, was tuned in simulation to produce an aircraft response that followed the rules outlined by Reichmann. The thermal model given in reference 18 was implemented into a hardware–in-the-loop simulation for controller evaluation and gain tuning. The k_1 and k_2 gains were tuned to make the path of the aircraft more circular and to improve the damping of the controller during soaring flight in a variety of thermal sizes and strengths. The resulting control gains were chosen to be 50, 0.4, and 0.165 for k_1, k_2, and k_3 respectively.

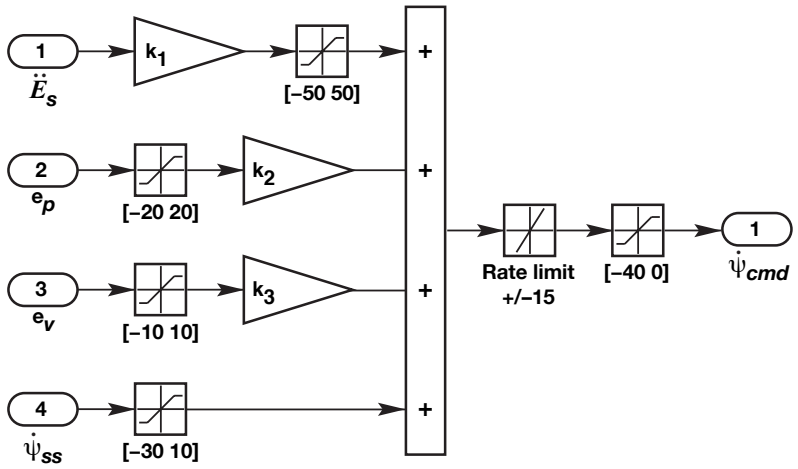

Figure 8. Soaring controller. Turn rate command output from soaring controller is tracked by the autopilot during soaring flight.

Mode Logic

Engagement and disengagement of the soaring controller during flight was handled autonomously using the mode logic shown in figure 9. The mode logic described in this section is significant because it determines how a thermal is detected and what conditions must exist before the aircraft will leave the thermal. The mode logic is broken into three components; thermal detection, thermal rejection, and a latch mechanism. The thermal detection logic uses aircraft response to detect thermals. An encounter with a thermal by the aircraft produces large changes in energy rate and energy acceleration. As the airplane flies a straight path through a typical thermal, the energy acceleration reverses sign and becomes negative when the aircraft is nearest to the center of the thermal. The thermal detection logic is tuned to trigger when the thermal is imputing significant energy to the aircraft and the aircraft is closest to the thermal center.

The decision to switch from soaring flight to searching flight was handled by thermal rejection logic using energy rate. Thermal rejection was needed to switch from soaring flight to searching flight when the thermal was no longer providing sufficient energy to the aircraft. Two energy-rate based criteria are used by the thermal rejection logic. First, thermals are rejected if the output of filter 4 is less than –0.5 m/s. This criterion would be met if the aircraft encountered light sink for a period of approximately 5 s. The second criterion, based on the output of filter 5, triggered if the aircraft had not experienced sufficient energy rate for approximately 10 s. Additional criteria, not shown in figure 9, were used to disengage from soaring mode when the upper or lower altitude limit was exceeded, a loss of communication between the UAV and ground station (lost link) occurred, or soaring mode was disabled by the ground station operator.

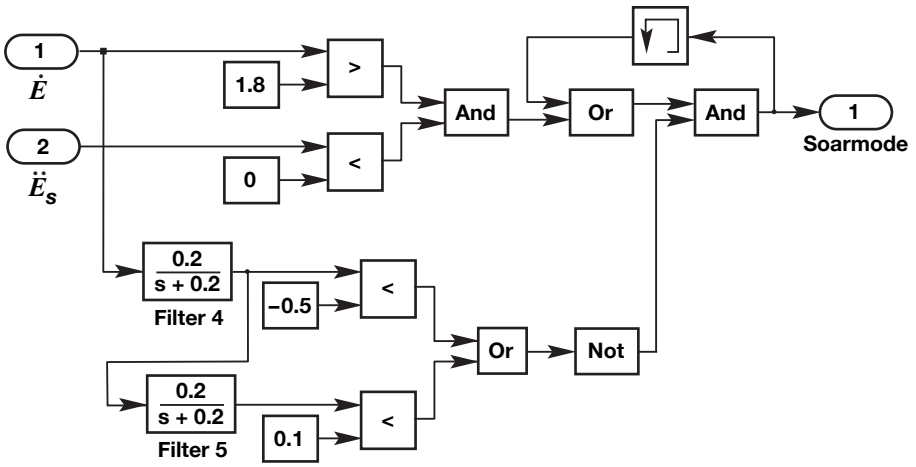

Figure 9. Mode logic diagram. The aircraft will enter soaring flight when Soarmode = 1.

RESULTS

A total of 17 flight tests with the Cloud Swift were conducted during the summer of 2005 to perform aircraft checkout, tune autopilot gains, and test the autonomous soaring guidance and control. Twenty-three thermals were detected and utilized during the soaring research flights. The average altitude gain obtained from a single thermal was 173 m (567 ft) as measured by the Piccolo Plus GPS.

The path of the aircraft during a typical soaring flight in an average thermal is shown in figure 10. The aircraft encounters two thermals during this time period. A small thermal at position $P_X = -900$ and $P_Y = 300$, was not sufficient to cause the mode logic to engage soaring mode. The second thermal encountered at $P_X = -1250$ and $P_Y = 100$ barely imparted sufficient energy to the aircraft to cause a mode change. The estimated thermal position, shown in black, moves as the aircraft encounters increasing or decreasing energy from the thermal. During soaring flight, the aircraft progresses in the positive X and Y direction (North and East) as the thermal drifts. The aircraft attempts to increase the time it spends in lifting air as it circles in a thermal that is likely varying with time and altitude.

Figure 11 shows the energy state of the aircraft for the flight path shown in figure 10. Controller performance was determined from the time history of energy rate. Energy rate should be constant when the aircraft is perfectly centered in the thermal. In this time history, energy rate fluctuates as the aircraft climbs in the thermal, indicating that improvements in the soaring algorithm can be obtained. Postflight estimated energy rate $\dot{E}_{pf}$, shown in the second subplot of figure 11, represents the true energy rate of the aircraft and was obtained by first forward-backward filtering the aircraft energy with a second-order low-pass filter and then differentiating the result. The onboard estimate of $\dot{E}$ differs from the postflight estimated $\dot{E}$ because the onboard estimate includes the delays caused by filter 1 and filter 2. The delay of the onboard estimate of $\dot{E}$ and $\ddot{E}$ resulted in reduced controller performance.

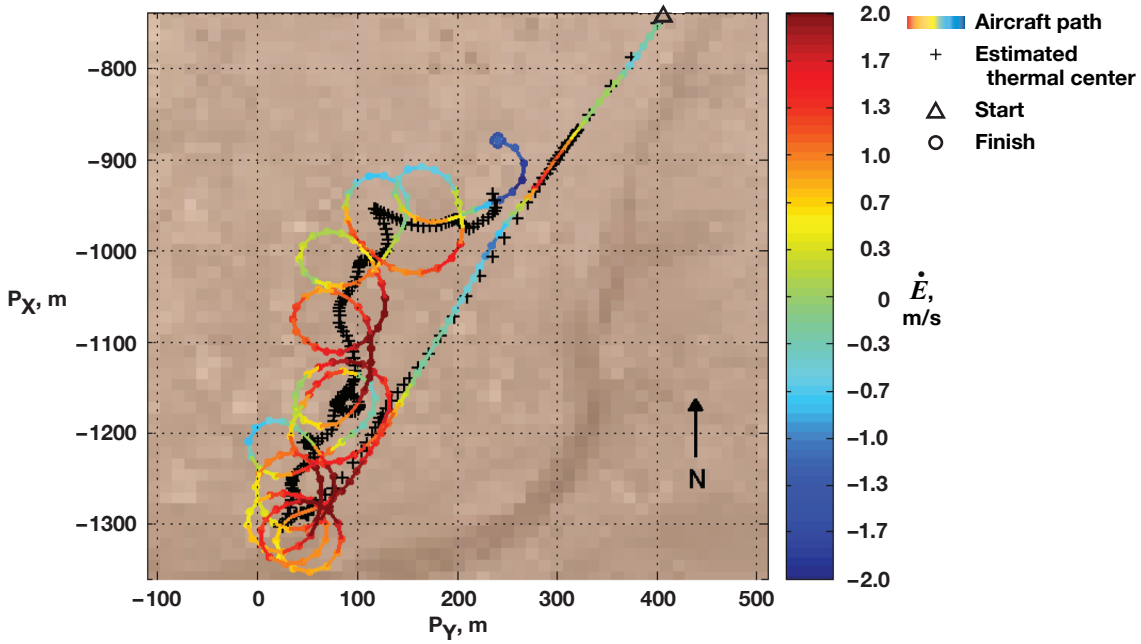

060390

Figure 10. Aircraft path during soaring flight in an average thermal. The aircraft starts at the upper right and flies in a straight line until a sufficiently strong thermal is detected at the bottom left corner of the figure.

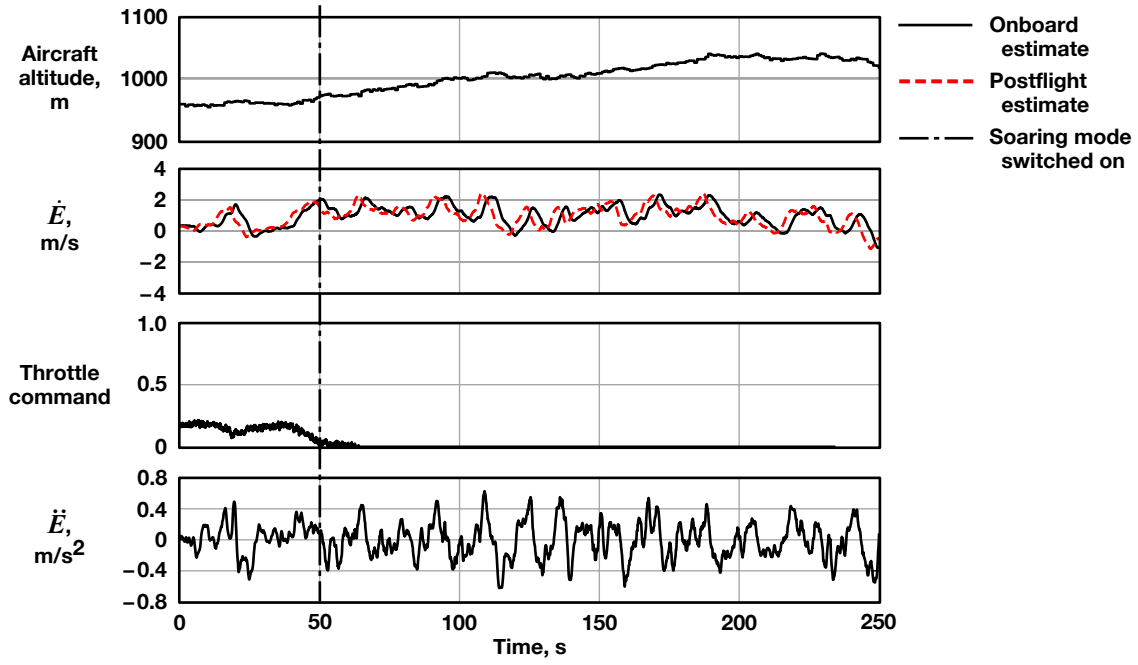

060391

Figure 11. Aircraft energy state during soaring flight in an average thermal.

Figure 11 also shows the throttle command drop to zero shortly after the thermal is encountered, indicating gliding flight with the propeller folded. The Piccolo Plus autopilot was configured to use the throttle to control altitude. This caused the throttle to go to zero and the propeller to fold back as the aircraft climbed above the commanded altitude while soaring.

The bank angle, pitch rate, and yaw rate are shown in figure 12 for the section of flight shown previously in figures 10 and 11. Variations in bank angle reveal the activity of the aircraft as it attempts to stay within the thermal.

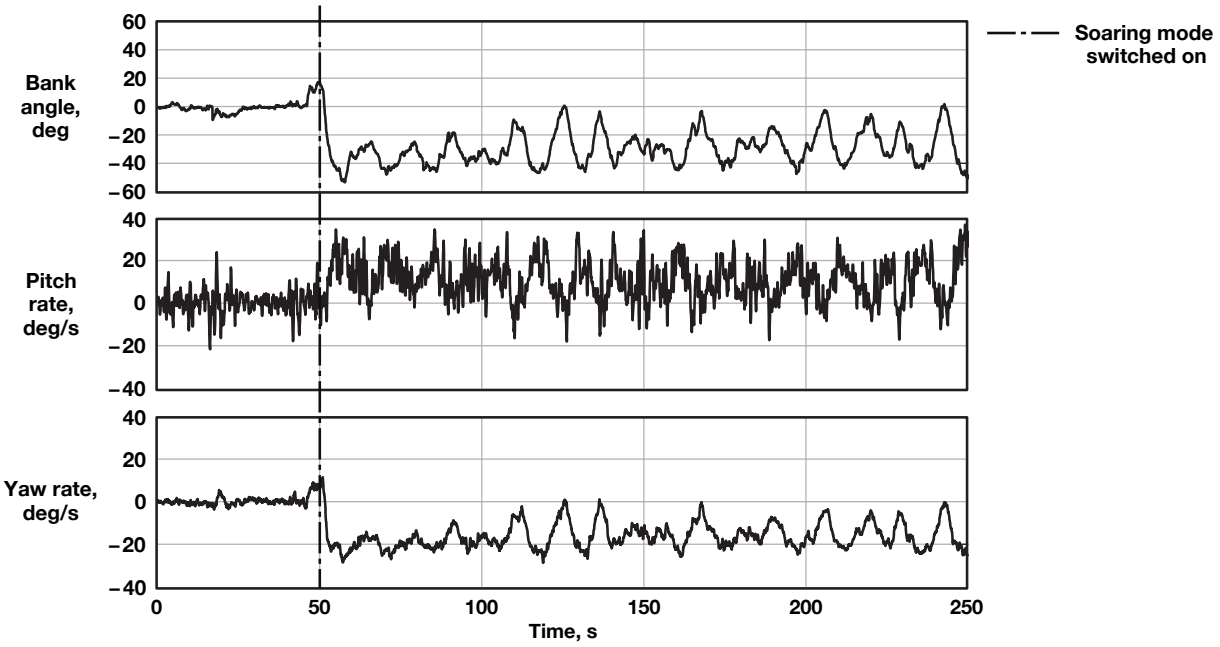

Figure 12. Aircraft states during soaring flight in an average thermal.

Thermal position estimation values are shown in figure 13 for the same thermal. Aircraft path and drift corrected path were taken from q_1 and q_2 respectively at 232 s. The figure shows increasing thermal velocity toward the right side of the drift corrected path causing the estimated thermal center to move in the positive direction. The distance of each position in q_2 to the estimated thermal center is plotted against the energy rate of each point in figure 14. The estimated thermal shape is also plotted in figure 14 to illustrate the performance of the thermal estimation algorithms. The figure shows that the basic shape of a thermal can be approximated by eq. (18); however, the estimated thermal shape did not fit the data perfectly, indicating that eq. (18) did not capture all of the properties of the thermal.

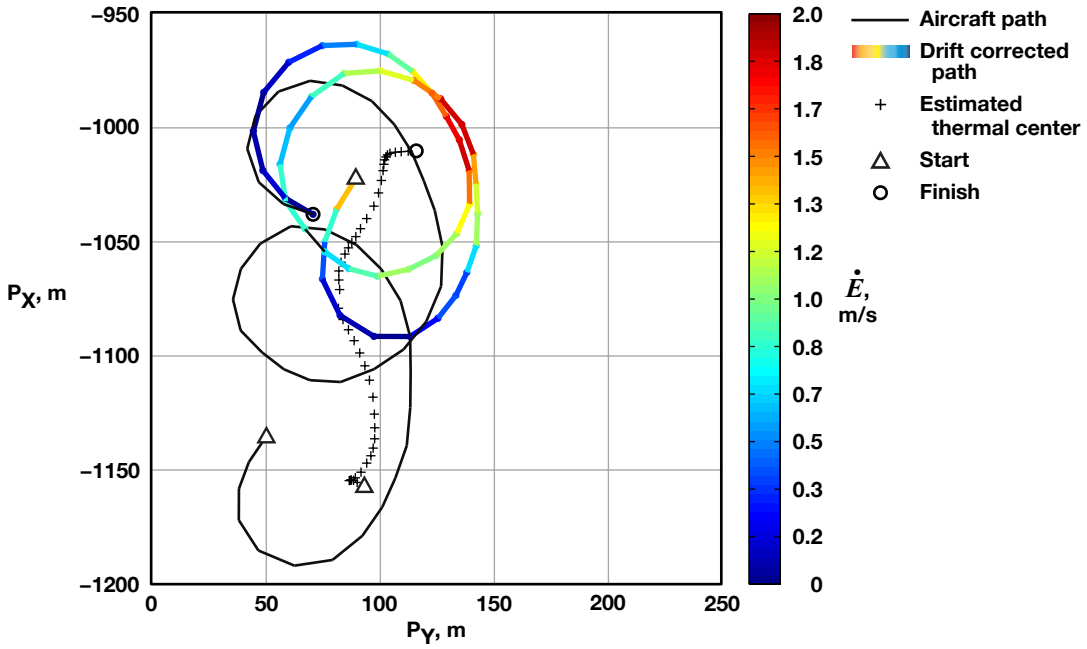

Figure 13. Thermal position estimation values for soaring flight in an average thermal. Aircraft path and drift corrected path values were taken from q_1 and q_2 respectively.

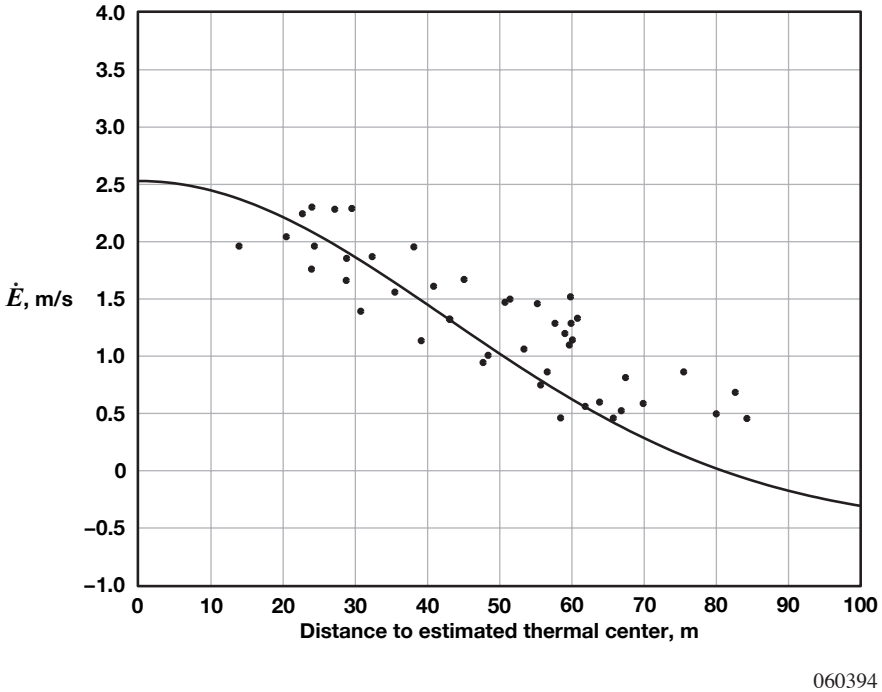

Figure 14. Thermal radius estimation values for flight in an average thermal. Estimated thermal velocity and radius is 2.52 m/s and 60 m respectively.

Figure 15 shows a failure of the UAV to detect and circle within a weak thermal. The mode logic in this case did not switch to soaring mode quick enough to allow the aircraft to stay within the lift. The switching delay was caused by two factors: the non-symmetrical shape of the thermal vertical velocity as the aircraft flew through the thermal and the delay in the energy rate and energy acceleration estimates. This problem can likely be remedied through better tuning of the mode logic and soaring controller and the use of an energy-state solution with less delay.

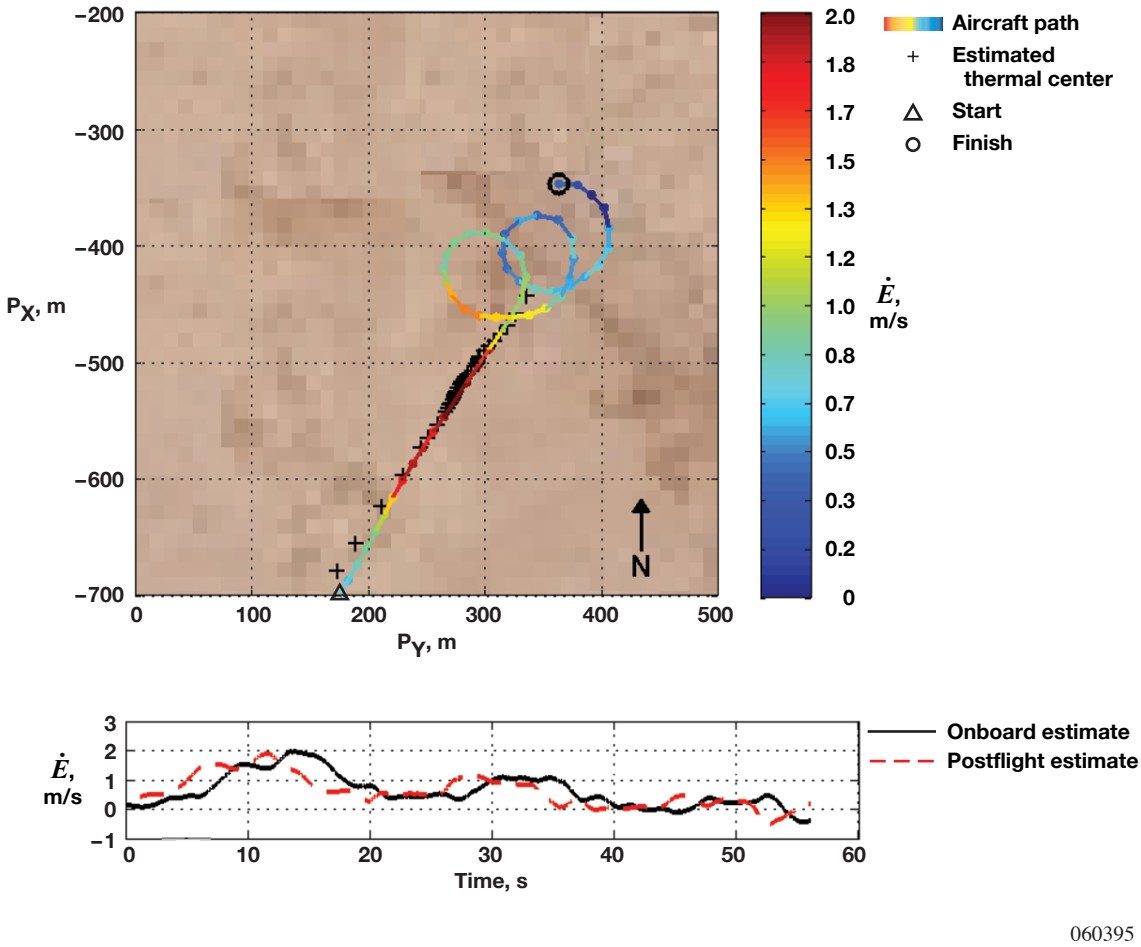

Figure 15. Example of a late mode switch into soaring mode.

The soaring controller was able to keep the energy rate more constant when soaring in a stronger thermal as shown in figure 16. The aircraft gained over 600 m (2000 ft) in this thermal, as reported by GPS, and experienced an average climb rate of 2.8 m/s (5.4 kn). The estimated thermal radius was saturated on the predefined upper limit of 80 m during this climb. Energy rate and acceleration delay may have had less impact on controller performance as the aircraft flew larger circles in stronger lift. Figure 17 shows the altitude gain along with a more constant $\dot{E}$ associated with improved controller performance.

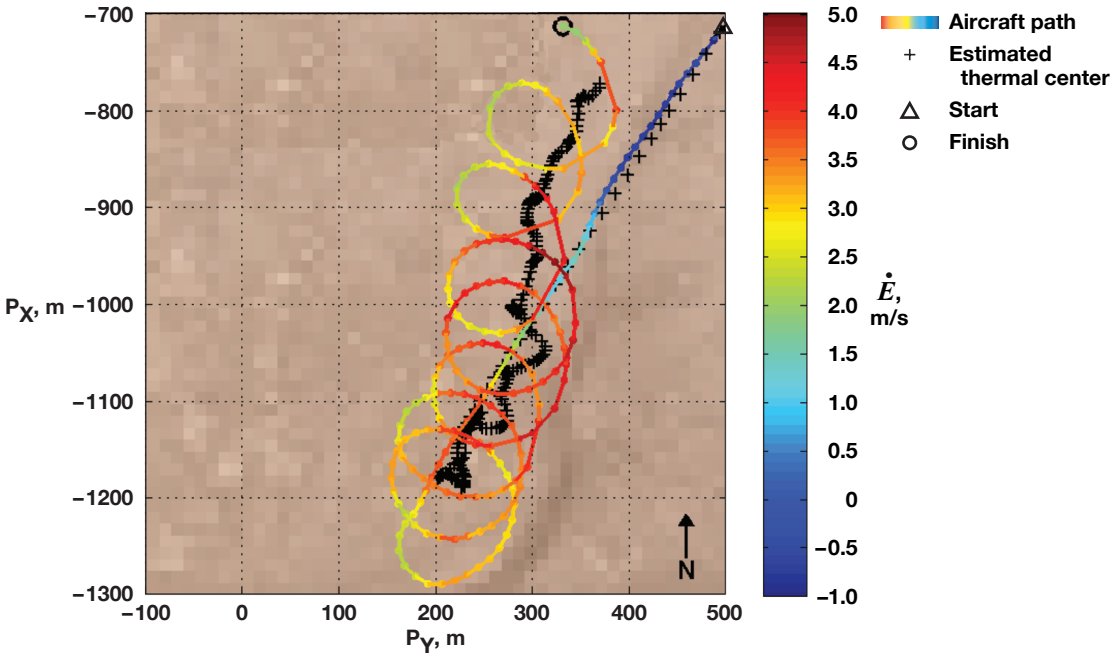

060396

Figure 16. Aircraft path and estimated thermal center during soaring flight in strong lift.

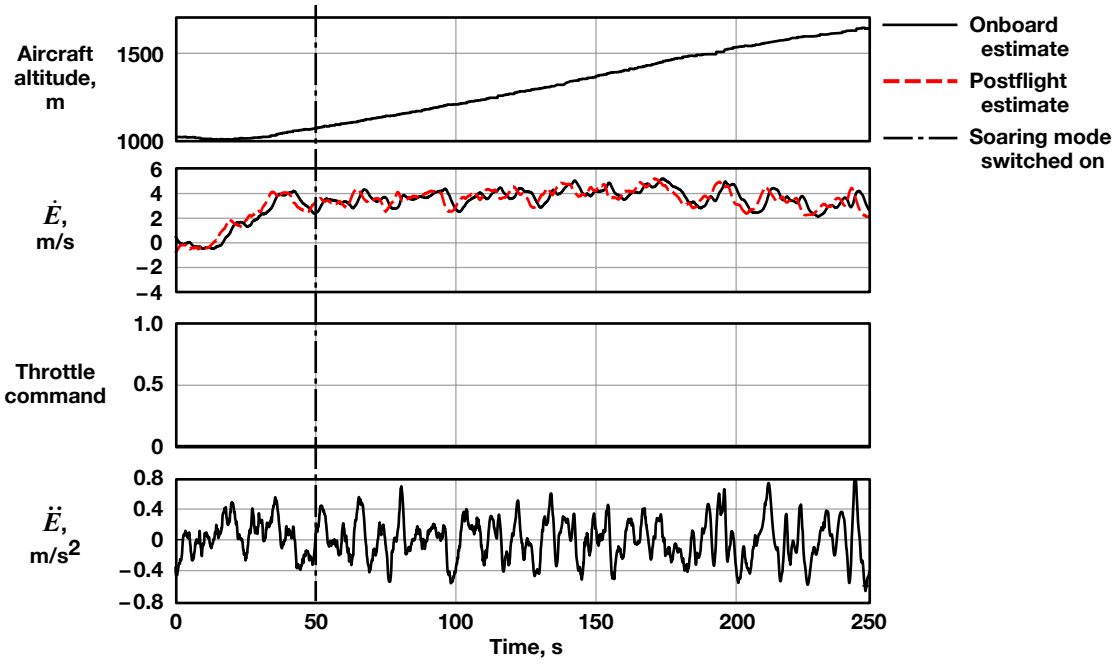

060397

Figure 17. Aircraft energy state during soaring flight in strong lift.

Although long duration flight was not an objective of this project, a partial demonstration of increased endurance is shown in figure 18. The top plot in figure 18 shows the altitude of the aircraft during one of the research flights. The cruise altitude for this flight was 960 m. The bottom plot shows throttle command where a value of 1 is full throttle, used for takeoff, and a value of 0 is power off, gliding flight. The altitude time history of the aircraft during this flight is similar to those predicted by simulation (ref. 6) and to those of migratory birds (ref. 4). The flight was ended when the capacity of the actuator batteries was consumed. Despite this limitation, the UAV flew over 60 min without using the motor during this flight.

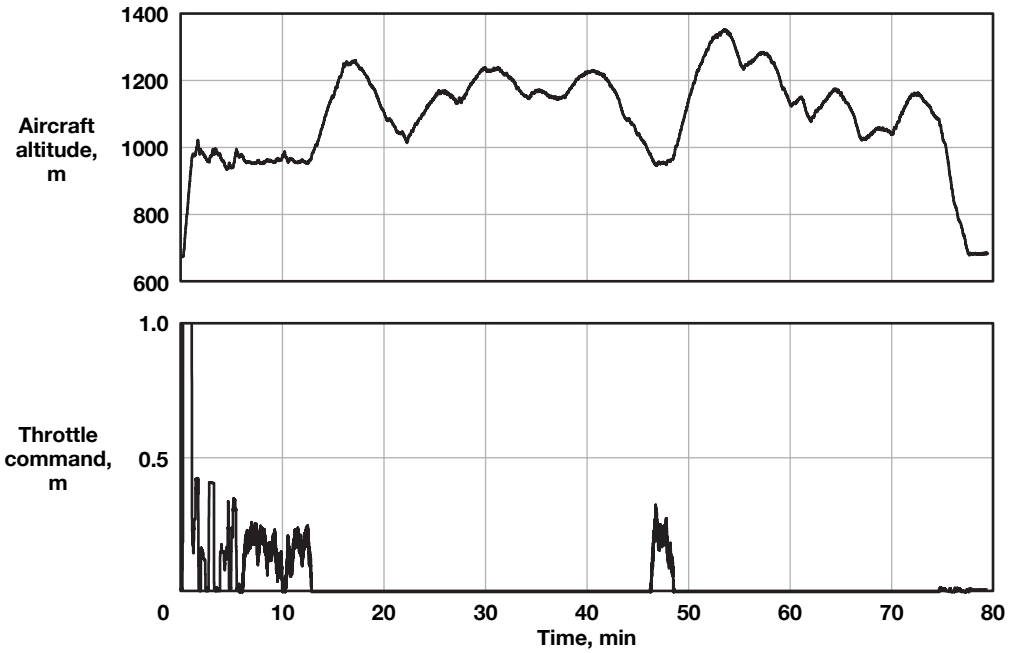

Figure 18. Extended soaring flight. Multiple thermals were used to glide under autonomous control for over 60 min. The flight was ended prematurely because the vehicle was not configured with actuator batteries for long endurance flight.

CONCLUDING REMARKS

A guidance and control method for autonomous soaring flight in thermal updrafts was developed and tested using a small electric-powered unmanned aerial vehicle. The total energy rate of the vehicle was estimated from static and total pressure measurements using digital filters and differentiators. The position, radius, and strength of the thermals were estimated using a history of total energy rate and aircraft position measurements contained in a first-in-first-out queue. Thermal drift velocity was estimated and used to map the aircraft position data in the queue to a reference frame attached to the thermal. The data in the queue was then used to estimate the thermal center location using a centroid calculation. The radius of the thermal was estimated using an iterative fit to an assumed thermal vertical velocity profile.

Aircraft velocity command, thermal position, and thermal radius were used to generate a circular flight path command for soaring. Position and velocity error to the flight path command were used along with calculated steady-state turn rate to generate a turn rate command in the soaring controller. The general structure and initial gain values of the soaring controller were taken from piloted soaring rules. Lastly, simple mode logic based on the aircraft energy state was used to engage and disengage the soaring controller.

The soaring algorithms were flight tested at Edwards Air Force Base using a 14-ft span electric-powered UAV. Results show that the UAV could autonomously detect and exploit thermals to gain altitude and conserve energy. Controller performance was determined by inspecting the unsteadiness of the aircraft energy rate during soaring flight. Controller performance was found to be better in strong thermals. Latency in energy rate and energy acceleration estimates was found to be the primary cause of reduced controller performance in weak thermals. Future soaring algorithms should use better pressure sensors or incorporate aircraft acceleration information to improve the energy state estimate. Although demonstration of long endurance flight was not an objective of this project, multiple thermals were used in a single flight to soar autonomously for over 60 min. Overall, the flight results show successful autonomous soaring of a small UAV using the algorithms given in this report.

REFERENCES

1. Welch, Ann, Lorne Welch, and Frank Irving, *New Soaring Pilot*, 3rd edition, Thomas Knauff, 1991.

2. Pennycuick, C. J., "Soaring Behaviour and Performance of Some East African Birds, Observed from a Motor-Glider," *IBIS 114*, 1972, pp. 178–218.

3. Kerlinger, Paul, *Flight Strategies of Migrating Hawks*, The University of Chicago Press, Chicago and London, 1989.

4. Shamoun-Baranes, Judy, Yossi Leshem, Yoram Yom-Tov, and Olivier Liechti, "Differential Use of Thermal Convection by Soaring Birds over Central Israel," *The Condor*, Vol. 105, The Cooper Ornithological Society, 2003, pp. 208–218.

5. Weimerskirch, Henri, Olivier Chastel, Christophe Barbraud, and Olivier Tostain, "Frigatebirds Ride High on Thermals," *Nature*, Vol. 421, Nature Publishing Group, January 23, 2003, pp. 333–334.

6. Allen, Michael J., "Autonomous Soaring for Improved Endurance of a Small Uninhabited Air Vehicle," AIAA-2005-1025, 2005.

7. Reichmann, Helmut, *Cross-Country Soaring*, 7th ed., Soaring Society of America, Inc., Hobbs, New Mexico, 1993.

8. Boslough, Mark B. E., "Autonomous Dynamic Soaring Platform for Distributed Mobile Sensor Arrays," SAND2002-1896, Sandia National Laboratories, 2002.

9. Patel, Chinmay K., and Ilan Kroo, "Control Law Design for Improving UAV Performance Using Wind Turbulence," AIAA-2006-0231, 2006.

10. Wharington, John, and Israel Herszberg, "Control of a High Endurance Unmanned Air Vehicle," ICAS-98-3,7,1, AIAA A98-31555, *21st ICAS Congress*, Melbourne, Australia, September 13–18, 1998.

11. Wharington, John, "Autonomous Control of Soaring Aircraft by Reinforcement Learning," Doctorate theses, Royal Melbourne Institute of Technology, Melbourne, Australia, 1998.

12. Kjerrström, Staffan, "The Thermal Computer and its Development," URL: http://hem.passagen.se/skj/engelska/utv.htm [cited 20 November 2006].

13. Cocconi, Alan, "AC Propulsion's Solar Electric Powered SoLong UAV," June 5, 2005, URL: http://www.acpropulsion.com/ACP_SoLong_Solar_UAV_2005-06-05.pdf [cited 20 November 2006].

14. Dornheim, Michael A., "Perpetual Motion," *Aviation Week & Space Technology*, June 27, 2005, pp. 48–52.

15. Murray, Charles J., "The Quest for Perpetual Flight," *Design News*, November 26, 2005, pp. 71–74.

16. U.S. Standard Atmosphere, 1962.

17. Telford, James W., "Convective Plumes in a Convective Field," *Journal of the Atmospheric Sciences*, Vol. 27, No. 3, May 1970, pp. 347–358.

18. Allen, Michael J., "Updraft Model for Development of Autonomous Soaring Uninhabited Air Vehicles," AIAA-2006-1510.

REPORT DOCUMENTATION PAGE

Form Approved
OMB No. 0704-0188

1. REPORT DATE *(DD-MM-YYYY)*	2. REPORT TYPE	3. DATES COVERED *(From - To)*
01-02-2007	Technical Memorandum	

4. TITLE AND SUBTITLE
Guidance and Control of an Autonomous Soaring UAV

5a. CONTRACT NUMBER

5b. GRANT NUMBER

5c. PROGRAM ELEMENT NUMBER

6. AUTHOR(S)
Allen, Michael J.

5d. PROJECT NUMBER

5e. TASK NUMBER

5f. WORK UNIT NUMBER

7. PERFORMING ORGANIZATION NAME(S) AND ADDRESS(ES)
NASA Dryden Flight Research Center
P.O. Box 273
Edwards, California 93523-0273

8. PERFORMING ORGANIZATION REPORT NUMBER
H-2682

9. SPONSORING/MONITORING AGENCY NAME(S) AND ADDRESS(ES)
National Aeronautics and Space Administration
Washington, DC 20546-0001

10. SPONSORING/MONITOR'S ACRONYM(S)
NASA

11. SPONSORING/MONITORING REPORT NUMBER
NASA/TM-2007-214611

12. DISTRIBUTION/AVAILABILITY STATEMENT
Unclassified -- Unlimited
Subject Category 08 Availability: NASA CASI (301) 621-0390 Distribution: Standard

13. SUPPLEMENTARY NOTES
Allen, Dryden Flight Research Center

14. ABSTRACT

Thermals caused by convection in the lower atmosphere are commonly used by birds and glider pilots to extend flight duration, increase cross-country speed, improve range, or simply to conserve energy. Uninhabited Aerial Vehicles (UAVs) can also increase performance and reduce energy consumption by exploiting atmospheric convection. An autonomous soaring research project was conducted at the NASA Dryden Flight Research Center to evaluate the concept through flight test of an electric-powered motor-glider with a wingspan of 4.27 m (14 ft). The UAV's commercial autopilot software was modified to include outer-loop soaring guidance and control. The aircraft total energy state was used to detect and soar within thermals. Estimated thermal size and position were used to calculate guidance commands for soaring flight. Results from a total of 23 thermal encounters show good performance of the guidance and control algorithms to autonomously detect and exploit thermals. The UAV had an average climb of 172 m (567 ft) during these encounters.

15. SUBJECT TERMS
Autonomy, Control, Convection, Soaring, Vertical air currents

16. SECURITY CLASSIFICATION OF:			17. LIMITATION OF ABSTRACT	18. NUMBER OF PAGES	19a. NAME OF RESPONSIBLE PERSON
a. REPORT	b. ABSTRACT	c. THIS PAGE			STI Help Desk (email: help@sti.nasa.gov)
					19b. TELEPHONE NUMBER *(Include area code)*
U	U	U	UU	31	(301) 621-0390